Interpretation of the horizontal beam response near the third integer resonance

E. C. Cortés García,[1,2,*] P. Niedermayer,[2] R. Singh,[2] R. Taylor,[3,4] E. Feldmeier,[5] M. Hun,[5] E. Benedetto,[6] and T. Haberer[5]

[1]*Deutsches Elektronen-Synchrotron DESY, Notkestraße 85, 22607 Hamburg, Germany*
[2]*GSI Helmholtz Centre for Heavy Ion Research, Planckstraße 1, 64291 Darmstadt, Germany*
[3]*CERN, Espl. des Particules 1, 1211 Meyrin, Switzerland*
[4]*Imperial College London, Exhibition Rd., South Kensington, London SW7 2BX, United Kingdom*
[5]*Heidelberg Ion-Beam Therapy Center, Im Neuenheimer Feld, 450, 69120 Heidelberg, Germany*
[6]*SEEIIST Association, Rue de Battoirs 7, 1205 Geneva, Switzerland*

(Received 4 April 2024; accepted 6 December 2024; published 30 December 2024)

The beam response to an external periodic excitation delivers relevant information about the optics, tune distribution, and stability of a circulating beam in a storage ring. In this contribution, the horizontal beam response to the excitation (transfer function) under conditions typical for slow extraction is presented for a coasting beam. The resulting spectrum exhibits a splitting behavior. The single particle dynamics is discussed and an interpretation based on the simulation results is presented.

DOI: 10.1103/PhysRevAccelBeams.27.124001

I. INTRODUCTION

Slow extraction from synchrotrons and storage rings is a well-established method to deliver a variety of beams to experiments and patients. In current versions of the method, the slow extraction is prepared by moving the horizontal working point near a third integer resonance while simultaneously reducing the dynamic aperture (DA) by driving the resonance with dedicated sextupoles. The effective horizontal dynamics under such conditions can be described by the Kobayashi Hamiltonian [1]. The beam is then extracted either by slowly reducing the DA further until it reaches zero or by slowly increasing the beam emittance beyond the (constant) DA. Different variations of this machine setup are in use [2–4]. In this contribution, the so-called radio frequency knock out (rf-KO) extraction is considered, which involves blowing-up the emittance through an external transverse excitation while keeping the DA constant [5].

In rf-KO extraction, the emittance blowup is achieved by applying an external rf electromagnetic field excitation. The amplitude of the betatron oscillations is thereby controlled and eventually increased beyond the DA, where particles become unstable and are pushed into the extraction channel. Several studies have been performed in order to engineer an optimal frequency spectrum for the rf excitation signal [6–11]; these studies have heavily relied on measured particle counts for trial-and-error optimization of the rf-signal spectrum. In this contribution, we take a step back and focus exclusively on the amplitude and phase response of the stored beam to an external sinusoidal excitation by measuring the beam transfer function (BTF) under extraction conditions. Here the sinusoidal stimulus replaces the usual rf excitation signal, but the rest of the machine setup remains the same as for rf-KO extraction.

Systematic studies of BTFs close to driven resonances are not to be found in the literature, to the best knowledge of the authors. The information gained by the BTF measurements has a significant application in the context of engineering an optimal waveform for the slow extraction [12,13], where fixed tone excitations have also been proposed [13].

Our contribution is organized as follows: In Sec. II, the particle dynamics under slow extraction conditions is reviewed together with the theoretical background of the extraction, for single and multiparticle dynamics. In Secs. III and IV, measurements and simulations of the beam response of a coasting beam are presented, respectively. We conclude with a summary and a discussion of the results in Sec. V.

II. THEORY

A. Single particle dynamics

The status-quo of the study of nonlinear dynamics relies on the Lie-algebraic formulation of transfer maps induced by Hamiltonians of different particle accelerator elements [14,15]. The workhorse for the engineering and optimization

*Contact author: edgar.cristopher.cortes.garcia@desy.de

of slow extraction via the third integer resonance is the Kobayashi Hamiltonian [1]. It is an approximate description of the particle dynamics when the tune Q_x is close to a third-order resonance Q_{res} driven by sextupole magnets. Comprehensive derivations and corollaries of this dynamics can be found in [16].

The Kobayashi Hamiltonian H for on-momentum particles reads

$$H = h_0 + h_1, \tag{1}$$

with

$$h_0 = -6\pi(Q_x - Q_{\text{res}})J_x =: -\delta J_x, \tag{2}$$

$$h_1 = -\frac{S}{\sqrt{2}} J_x^{3/2} \sin 3\phi_x, \tag{3}$$

where action-angle variables (J_x, ϕ_x) are used, which relate to the horizontal space coordinate x as $x = \sqrt{2\beta_x J_x}\sin\phi_x$ [15–17]. Along our contribution, the fractional part of the linear (zero-amplitude) tune will be represented by $q_{x,0}$, such that $Q_x = n + q_{x,0}$ with $n \in \mathbb{N}_0$. Q_{res} is the closest third integer resonance ($3Q_{\text{res}} \in \mathbb{N}$). Moreover, S can be interpreted as the amplitude of the resonance driving term excited by an effective single virtual sextupole. The virtual sextupole strength S is given by

$$S = \left| \sum_n^N S_n e^{-i3\mu_n} \right|, \tag{4}$$

with

$$S_n = \frac{1}{2} \int \beta_x^{3/2} k_2 \mathrm{d}s, \tag{5}$$

where N is the total number of sextupoles in the lattice, $\mu_n = \int_0^{s_n} \beta_x^{-1} \mathrm{d}s$ the betatron phase advance to the nth sextupole, and $k_2 = \frac{1}{B\rho}\frac{\partial^2 B_y}{\partial x^2}$ the normalized sextupole field component. The integration of Eq. (5) is to be carried out along the sextupole's length. The phase advance of the virtual sextupole with respect to the arbitrary lattice start is given by

$$\tan 3\mu_S = \frac{\sum_n^N S_n \sin 3\mu_n}{\sum_n^N S_n \cos 3\mu_n}. \tag{6}$$

Figure 1 depicts the equipotential lines of H in normalized phase space in the range where stable motion is possible. Note that the phase space is shown at the position of the virtual sextupole μ_S with $S > 0$. This phase space structure is found in any machine, where the Kobayashi Hamiltonian governs the single particle dynamics.

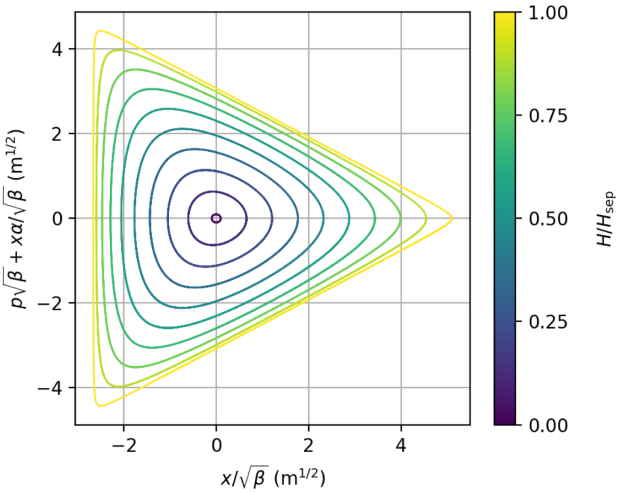

FIG. 1. Equipotential lines in the stable region of normalized phase space induced by the Kobayashi Hamiltonian. The value of the Hamiltonian at the separatrix edge reads $H_{\text{sep}} = [4\pi(Q_x - Q_{\text{res}})]^3/S^2$ [16].

1. Amplitude-phase-detuning

Since H describes the effective motion of a particle every three consecutive turns, by using the Lie-algebraic treatment [15,18], the amplitude-phase-dependent tune averaged over three consecutive turns is given as

$$q_x = q_{x,0} + q_{x,1} = \frac{1}{6\pi}\frac{\partial H}{\partial J_x} + q_{\text{res}}, \tag{7}$$

where $q_{x,0}$ is the unperturbed tune given by the linear theory, and

$$q_{x,1} = q_{x,1}(J_x, \phi_x) = \frac{3S}{\sqrt{2^5}\pi} J_x^{1/2} \sin 3\phi_x \tag{8}$$

is the amplitude-phase-dependent tune shift due to the nonlinear dynamics averaged over three turns. It is common

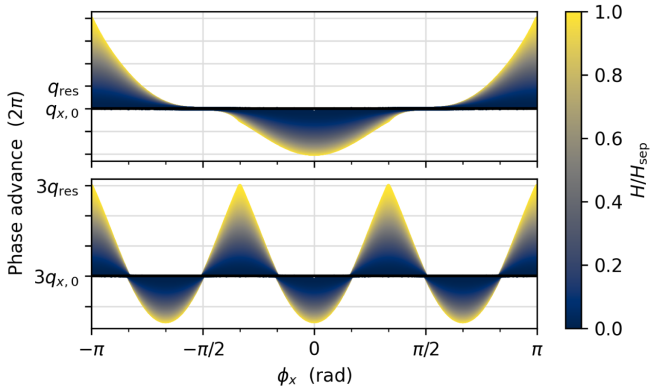

FIG. 2. Single (top) and three turn phase advance (bottom) as function of angle ϕ_x, colored by the value of the Kobayashi Hamiltonian H.

to apply averaging techniques over ϕ_x to Eq. (8) and intuitively, the contribution from the phase-amplitude detuning for a nearly constant action J_x should vanish.

However, near a resonance the phase space is deformed as the Kobayashi Hamiltonian clearly shows (Fig. 1), and the action J_x is *not* an invariant of motion [19]. Rather, it is a function of the angle $J_x = J_x(\phi_x)$ and as such modulated even without the effect of an external excitation. This is an important aspect: the phase advance of a single particle is not constant in time but varies as a function of the angle as the particle revolves in phase space. The resulting phase-advance modulation is illustrated in Fig. 2. As discussed later, this aspect determines how the particle responds to a sinusoidal excitation at a certain frequency over time.

Moreover, the single particle detuning can be better understood by investigating its long term average behavior [20]. The time average of a system's quantity g is given by $\langle g \rangle = \int_{t_1}^{t_2} g\mathrm{d}t / \int_{t_1}^{t_2} \mathrm{d}t$. Thus, the average three-turn phase advance $\langle \mu_3 \rangle$ yields [20]

$$\frac{\langle \mu_3 \rangle}{6\pi\delta} = \left(\frac{1}{2\pi} \int_0^{2\pi} \frac{\mathrm{d}\phi_x}{1 - \sqrt{2\tilde{J}}\cos 3\phi_x} \right)^{-1}, \tag{9}$$

where the normalized action $\tilde{J}$

$$\tilde{J} = \frac{J}{2J_{\max}} = \frac{J}{4(4\pi\delta)^2/S^2} = \begin{cases} \tilde{H}/6 & \text{if } \cos 3\phi_x = 0 \\ \frac{6 + R^{1/3}(\sqrt{3}i - 1) + R^{-1/3}(\sqrt{3}i + 1)(8\tilde{H}\cos^2(3\phi_x) - 9)}{16\cos^2(3\phi_x)} & \text{otherwise} \end{cases}, \tag{10}$$

$$R = 27 - 36\tilde{H}\cos^2(3\phi_x) + 4\tilde{H}^2\cos^3(3\phi_x)\left(2\cos(3\phi_x) - \sqrt{2\cos(6\phi_x) + 2 - 4/\tilde{H}}\right),$$

and the normalized effective energy

$$\tilde{H} = \frac{H}{H_{\text{sep}}} = \frac{H}{(4\pi\delta)^3/S^2} \tag{11}$$

were introduced.

$\tilde{J} = \tilde{J}(H, \phi_x)$ is expressed only as a function of the energy and the phase [20]. The right-hand side of Eq. (9) is unity for $\tilde{J} \to 0$ and thus the average three-turn phase advance is consistent with the linear theory. When the particle approaches the limit of $H \to H_{\text{sep}}$ then, in the corners of the stable phase space area where $\phi_x \to 0, \pi/3$ or $2\pi/3$, $\tilde{J}$ acquires the value of 1/2 while $\cos 3\phi_x$ becomes unity. Hence, the integral in Eq. (9) diverges and the average phase advance freezes, i.e., the particle hits the resonance $\langle \mu_3 \rangle \to 0$. The behavior of the average detuning over many turns is illustrated in Fig 3. It is clearly visible that the average three-turn phase advance detunes toward the nearest third-order resonance. The effect is more drastic when the energy of the particle is closer to the edge of the separatrix.

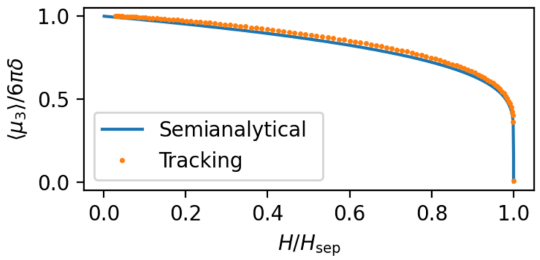

FIG. 3. Average three-turn phase advance as a function of the Hamiltonian. The solid blue line shows the value of Eq. (9), while the orange dots show the result of a single particle tracking of an FODO cell with a sextupole ($S = -30$) with $\delta = -2.5 \times 10^{-3}$ for 3300 turns.

2. External excitation

A couple of archetypes of externally driven nonlinear oscillator systems have been extensively studied, e.g., the Duffing equation, the forced Van-Der Pol oscillator [21], or Chirikov's standard map [22], to mention a few of the most prominent. In the context of particle accelerators, considerable progress on the theory of externally driven nonlinear systems has been done [23,24], where the introduction of external sinusoidal excitations provide useful schemes to either trap in nonlinear resonance islands fractions of the beam or to diffuse the beam in an rf abort case. Following the Lie-algebraic treatment, the effective time-dependent one-turn Hamiltonian of our system reads [15]

$$H(n) = -\mu_x J_x - \frac{h_1}{3} + A_x J_x^{1/2} \sin\phi_x \sin(\Omega n) - \mu_x \frac{S}{\sqrt{2}} J_x^{3/2}\left(\frac{1}{3}\cos 3\phi_x + \cot\frac{\mu_x}{2}\sin\phi_x + \cos\phi_x\right), \tag{12}$$

where $\mu_x = 2\pi q_{x,0}$ is the one-turn phase advance, A_x is the normalized strength of the external periodic excitation, Ω represents its frequency, and n is the turn number. In this case, the system does not resemble any of the archetypes.

B. Collective dynamics: Beam response

The study of the collective response of an ensemble of oscillators under the influence of an external weak force $f_x(t) = \epsilon\cos(\Omega t)$ can be found in literature for the analysis

of beam instabilities and study of tune spectra (see, e.g., [25,26]). The amplitude of the beam centroid oscillation $\langle x \rangle$ as a function of the driving frequency (approximately) reads [27,28]

$$\langle x \rangle(t) = \frac{\epsilon}{2\mu_x}\left[\cos \Omega t \, \mathcal{P}.\mathcal{V}. \int \mathrm{d}\mu \frac{\rho(\mu)}{\Omega - \mu} + \pi\rho(\Omega) \sin \Omega t\right], \tag{13}$$

where ϵ is the normalized strength of the force, $\rho(\mu)$ is the distribution function of the frequencies of the oscillator ensemble, $\mu_x = 2\pi q_{x,0}$ is the linear betatron frequency (assumed to be the mean value of the distribution), and $\mathcal{P}.\mathcal{V}.$ denotes the principal value of the integral. Equation (13) is valid when $\rho(\mu)$ only peaks once and the transversal motion of the oscillators do not influence $\rho(\mu)$ itself. For the case where the oscillators in the ensemble experience, a linear detuning as a function of their action J_x a similar result is known [29,30].

Hence an analytical expression is known for the beam transfer function (BTF) $T(\Omega)$

$$T(\Omega) = f(\Omega) + ig(\Omega), \tag{14}$$

with the conventional definitions

$$f(\Omega) = \mathcal{P}.\mathcal{V}. \int \mathrm{d}\mu \frac{\rho(\mu)}{\Omega - \mu}, \qquad g(\Omega) = \pi\rho(\Omega).$$

Note that the beam centroid oscillation amplitude [Eq. (13)] is directly related to the BTF by

$$\langle x \rangle(t) = \Re\left[\frac{\epsilon}{2\mu_x} \exp(-i\Omega t) T(\Omega)\right]. \tag{15}$$

For a system where the nonlinear dynamics near a resonance are prevalent, there is no known analytical or semianalytical expression for the BTF. Therefore, we investigate experimentally the beam centroid oscillation amplitude to an external sinusoidal excitation under the aforementioned conditions. In the following, we will refer to $\langle x \rangle / \epsilon$ as the beam response to the excitation frequency Ω.

III. BEAM RESPONSE MEASUREMENT

Measurements of the beam response under resonant slow extraction conditions were carried out at the Heidelberg Ion-beam Therapy Center (HIT) in 2022. In this section, the measurement setup and experimental results are presented. Before we continue, we would like to introduce some nomenclature. Hereinafter, we will refer to the on-momentum eigenfrequency, where $S = 0$, as the betatron resonance. This resonance can be excited at any frequency [31]

$$f_\beta^{n\pm} = f_{\mathrm{rev}}(n \pm q_{x,0}), \qquad n \in \mathbb{N}_0, \tag{16}$$

where we refer to $f_\beta^{n\pm}$ as the nth betatron sideband. The nth betatron sideband possesses an upper $f_\beta^{n+} = f_{\mathrm{rev}}(n + q_{x,0})$ and a lower $f_\beta^{n-} = f_{\mathrm{rev}}(n - q_{x,0})$ frequency. The experimental results of the beam response to excitation frequencies near two betatron sidebands—the upper ninth f_β^{9+} and the lower eighth f_β^{8-}—will be presented.

A. Experimental setup

1. Heidelberg Ion-Therapy Center synchrotron

The Heidelberg Ion-Beam Therapy Center (HIT) is a medical accelerator facility dedicated to the treatment of cancer tumors in patients with light ions (p^+, He^{2+}, C^{6+}, and O^{6+}) using the intensity controlled raster scan [32,33]. The HIT synchrotron layout is illustrated in Fig. 4. It is a compact machine with a circumference of 64.96 m. The ring is composed of two super cells each with three quadrupole doublet sections. Each super cell is equipped with two families of sextupole magnets, one optimally placed for chromaticity correction and the other one for the excitation of the resonance driving term. The optical functions of the synchrotron at extraction conditions are depicted in Fig. 5.

The measurements are carried out with a carbon-ion beam $^{12}C^{6+}$ with $E_{\mathrm{kin}} = 124.25$ MeV/nucleon. There was a dedicated measurement campaign to characterize the

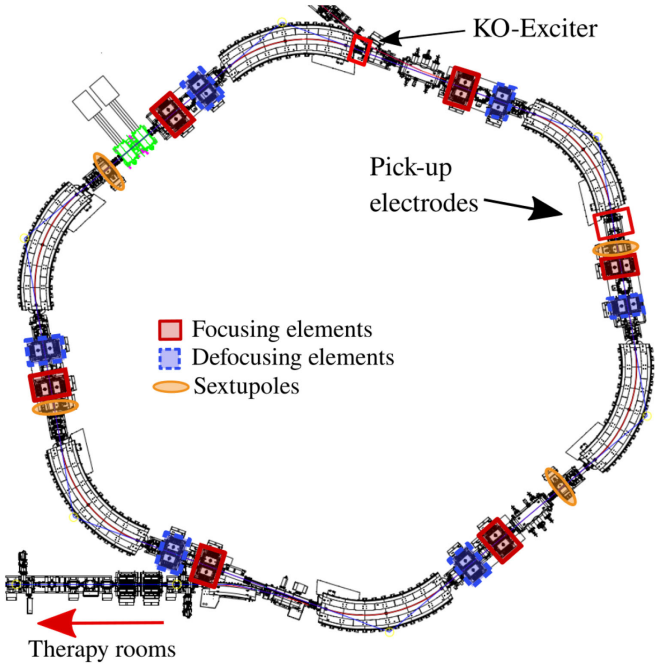

FIG. 4. The Heidelberg Ion-beam Therapy Center's synchrotron. The position of the (de)focusing quadrupoles are indicated with (blue)red boxes. The position of the sextupoles are indicated with an orange ellipse. The injection channel can be seen in the top middle, whereas the extraction to the therapy rooms is visible in lower left corner.

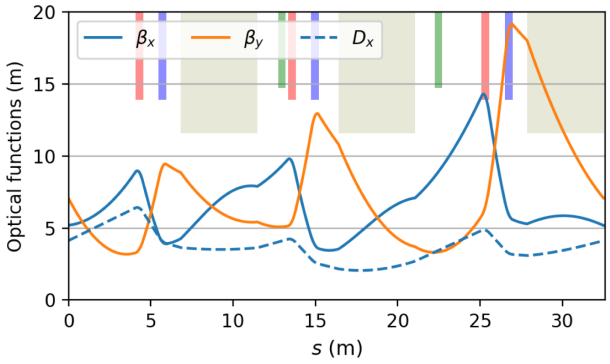

FIG. 5. Optical functions of the HIT's synchrotron super cell at extraction conditions. The solid curves show the transversal β-functions, whereas the dashed line illustrates the horizontal dispersion D_x. The position of the (de)focusing elements are marked with a red(blue) box on the top. The green marks indicate the position of the sextupoles. The dipoles are illustrated with a wide box.

linear optics of the machine and the beam properties relevant for the study. An extended description of these measurements can be found in Appendix A. Unfortunately, the beam diagnostics at HIT do not enable the direct measurement of the transverse emittance of the coasting beam, hence this has to be kept as a free parameter. The measured machine and beam parameters are listed in Table I.

2. Beam response measurement setup

The beam response to an external excitation is measured with a vector network analyzer (VNA). The stimulus signal is connected to the amplifier of the regular KO-exciter, providing transverse kicks to the beam. These sinusoidal kicks are of the form $\Delta x' = k_0 l \sin(2\pi f_{\mathrm{ex}} t + \varphi_{\mathrm{ex}})$ with the stimulus frequency $f_{\mathrm{ex}} = q_{\mathrm{ex}} f_{\mathrm{rev}}$ and phase φ_{ex}. The estimated transverse kick amplitude due to a given input stimulus power can be found in Table II. The stimulus leads finally to transverse oscillations of the beam centroid, which are recorded with regular capacitive pick-up electrodes in difference mode.

TABLE I. Measured machine and beam parameters for the beam response measurements. The model values come from a calculation from MADX [34]. The uncertainties of the measured values are listed in parenthesis.

Parameter	Symbol	Value	Model
Tunes	Q_x/Q_y	1.679(1)/1.720(1)	1.679/1.755
Chromaticity	ξ_x/ξ_y	$-2.85(3)/-2.80(3)$	$-1.78/-1.35$
Slip factor	η	0.46(3)	0.47657
Momentum spread (rms)	$\Delta p/p$	0.5×10^{-3}	
Revolution frequency	f_{rev}	2.1721 MHz	
Intensity	N_P	8×10^7 particles	

TABLE II. Estimated maximum kick for a given input stimulus power with a $^{12}C^{6+}$ carbon-ion beam with $E_{\mathrm{kin}} = 124.25$ MeV/nucleon. The values were estimated with an FEM simulation of the HIT KO-electrodes.

Input power (dBm)	Kick
0	1.54 μrad
−10	486 nrad
−20	154 nrad
−30	48.7 nrad

This provides the amplitude and phase-dependent signal to the VNA, which calculates the system response at the stimulus frequency. The setup is depicted in Fig. 6. Each measurement was carried out in a single machine cycle, where the stimulus frequency was swept over the course of 10 s, during which 701 frequency steps were probed. All the beam response measurements presented here were performed with a coasting (unbunched) beam.

B. Experimental results

The beam response was measured in the vicinity of the upper ninth f_β^{9+} and the lower eighth f_β^{8-} betatron sidebands [see Eq. (16)]. The integrated strengths of the sextupole magnets $k'_S L_S$ were varied in order to achieve a variation in the effective sextupole strength S [see Eq. (4)].

The results are illustrated in Fig. 7 for an excitation span near f_β^{9+}. The data shown were intentionally displaced (staggered) for better visualization of the details. Note that for the corrected chromaticity case (lower panel) for $S = 32$ m$^{-1/2}$ and 38 m$^{-1/2}$ the magnitude response was multiplied by a factor of two. The phase response for these measurements overlap considerably due to noise and is, therefore, not presented in Fig. 7. An example of the phase response with $S = 32$ m$^{-1/2}$ is shown in Fig. 8. The region

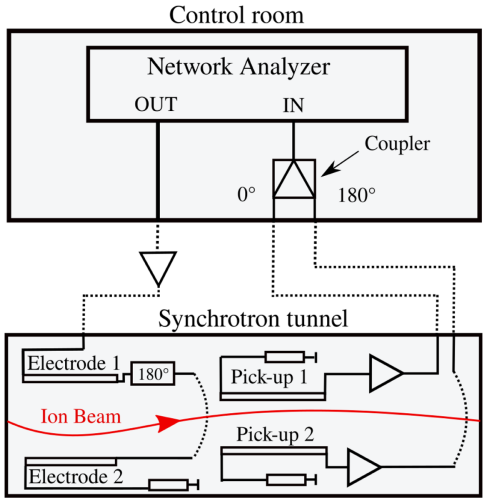

FIG. 6. Schematic of the experimental setup at HIT for the measurement of the beam response to an external excitation.

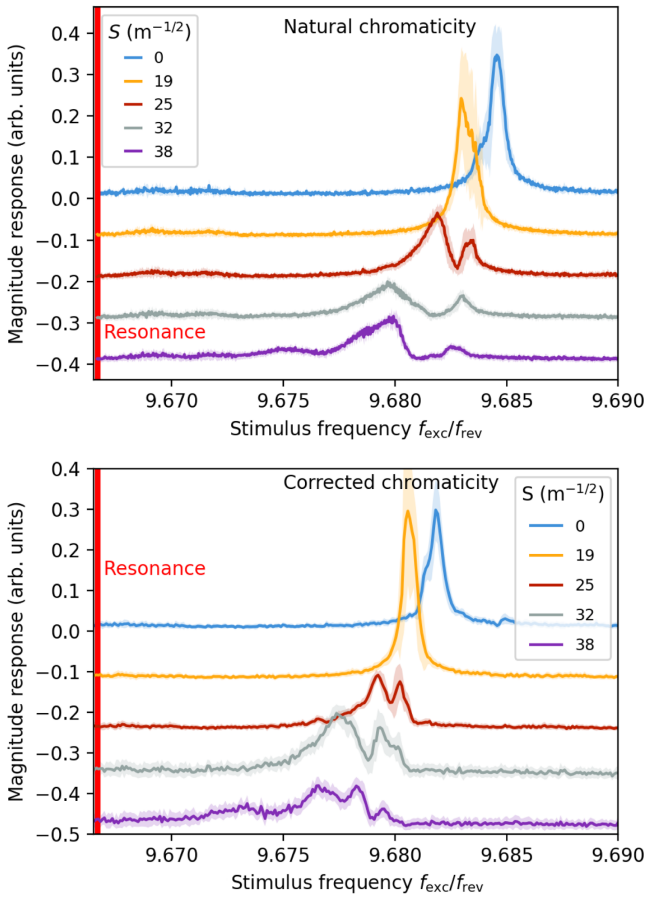

FIG. 7. Beam response measurement as function of sextupole strength at the upper ninth betatron sideband, with natural chromaticity (top) and fully compensated horizontal chromaticity (bottom). The stimulus frequency is scanned from the resonance (red line) to higher frequencies with a strength of −30 dBm ($k_0 l = 48.7$ nrad). Each graph composes the average and standard deviation over 25 cycles. The data was intentionally staggered in magnitude response. For $S = 32$ m$^{-1/2}$ and 38 m$^{-1/2}$ it was multiplied by a factor of two for the corrected chromaticity case for better visualization.

where the magnitude response splits exhibits fluctuations in the phase. For $S \leq 19$ m$^{-1/2}$, the beam response is very similar. Both of the curves are in the regime where the transversal dynamics are dominated by h_0 from Eq. (1), the motion resembles a linear oscillator and the nonlinearity still does not play an important role. Once $S \geq 25$ m$^{-1/2}$, the beam response starts splitting and exhibits two predominant maxima or one characteristic dip, respectively. The higher the value of S is set, the wider the gap between the two peaks becomes. It is also evident that the mean value of the beam response shifts toward the third-order resonance. This behavior comes both from the amplitude-phase detuning expected from the underlying dynamics described by Eq. (9), as well as from a contribution from the closed orbit at the sextupoles. The estimated closed orbit rms is 5 mm with a max/min excursion of 8 mm/ − 15 mm.

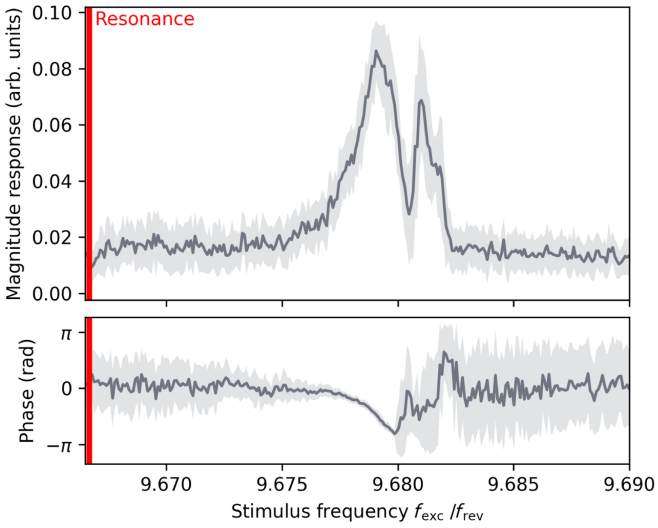

FIG. 8. Average beam response (solid curve) measurement of 25 machine cycles with $S = 32$ m$^{-1/2}$ from the sextupole strength scan with corrected chromaticity. The rms of the measurements is shown as the shaded area.

The same sextupole scan was performed and the beam response was measured at f_β^{8-}. The results are shown in Fig. 9. The behavior observed at this band is similar to f_β^{9-}. An exemplary measurement is included in Appendix B. Additionally, the measured phase response exhibited strong fluctuations as the upper ninth sideband. Thus the data are not shown. For $S \leq 19$ m$^{-1/2}$, there is one single peak in the beam response, indicating that the motion is governed by the linear dynamics. Above this threshold, the nonlinearity

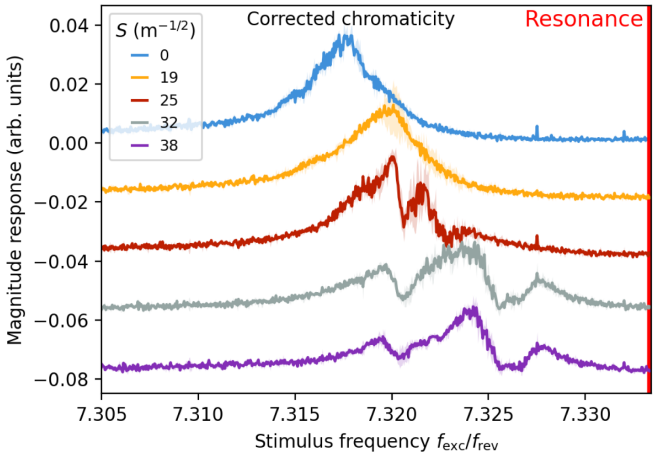

FIG. 9. Beam response measurement as function of sextupole strength at the eighth lower harmonic of the betatron resonance, with fully compensated horizontal chromaticity. The stimulus frequency is scanned from lower frequencies toward the resonance (red line) with a strength of −10 dBm ($k_0 l = 486$ nrad). Each graph composes the average and standard deviation over three cycles. The data were intentionally staggered for better visualization.

induces a splitting in the measured beam response. In this case, one can recognize more than two maxima or, respectively, at least one characteristic dip. The measurement of the beam response at f_β^{8-} and f_β^{9+} weas performed with the stimulus frequency spanning from the lower end to the higher end of the frequency span corresponding to each setting. This means that in the case of f_β^{9+} shown in Fig. 7, the stimulus frequency went first through the third-order resonance (highlighted as a vertical line in red on the left), then through the betatron resonance and continued to the higher end of the span. On the contrary, for the scan near f_β^{8-} shown in Fig. 9, the stimulus started with a frequency far from the resonance, then passed through the betatron resonance, and ended at the third-order resonance. This is an important aspect of the measurement that has to be considered, since the expected detuning due to the nonlinear dynamics only shifts the single particle tune toward the resonance. In other words, the direction of the excitation sweep can lead to different dynamics.

Finally, the dependency on the stimulus power of the beam response was measured near f_β^{9+} as well. The results are shown in Fig. 10, where the upper panel shows a broad scan in the stimulus frequency with the different curves showing the variation of the stimulus power (see Table II for the corresponding kick amplitude). The red line indicates the position of the nearest third-order resonance. The gray dashed lines indicate the approximate expected positions of different betatron resonance bands. The lower panel shows the phase with regard to the stimulus.

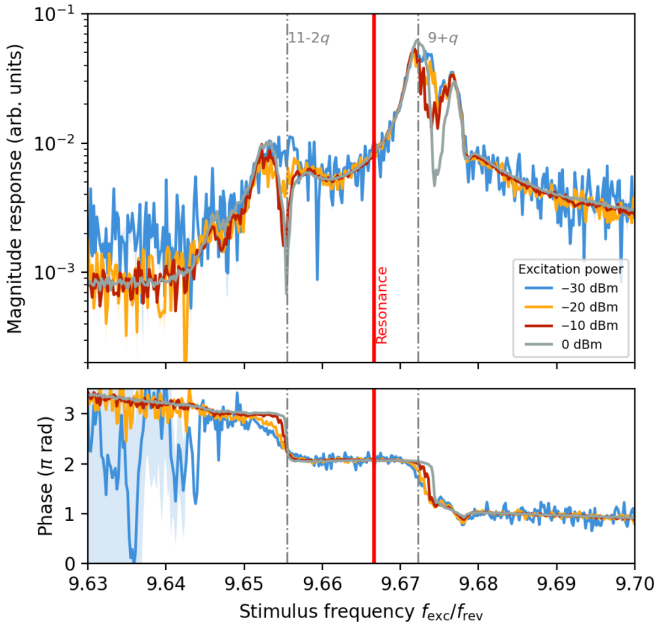

FIG. 10. Beam response with a $S = 32\ \mathrm{m}^{-1/2}$ for different input stimulus strengths. The dash-dotted lines indicate which resonance the peaks correspond to. The double peak structure becomes stronger with increasing excitation power.

The phase jumps are clear when the frequency crosses the dip in the magnitude response. Note that the phase response data was intentionally unwrapped.[1] By increasing the input power of the stimulus, which corresponds to an increasing strength of the kick amplitude that the beam experiences, the dip imprints deeper in the measured beam response. There is a noticeable shift of the measured response to values closer to the third-order resonance, when comparing to the results shown in Fig. 7. We attribute this shift to the influence of the excitation on the tune distribution due to the frequency sweep first going through the second order betatron sideband [36].

We note at the end of this section that the experimental results shown have been verified in various machines and with various beams. Some of these measurements are included in Appendix B.

IV. BEAM RESPONSE SIMULATION

The simulation of the beam response measurement is performed by launching a campaign of particle tracking computations to recover the horizontal beam oscillation amplitude. The particle tracking is performed with XSUITE [37]. The closed orbit corrector strengths are included in the model. A set with $N_p = 10^5$ particles is initialized, where each particle is described by an initial six-dimensional state vector $\vec{z}$. The transverse set of conjugate pairs (x, p_x) and (y, p_y) is initialized such that their probability density function is described by a stationary two-dimensional Gaussian distribution. i.e., the initial distribution's covariance matrix is given by

$$\Sigma_{x,y} = \varepsilon_{x,y} \begin{pmatrix} \beta_{x,y} & -\alpha_{x,y} \\ -\alpha_{x,y} & \gamma_{x,y} \end{pmatrix}, \tag{17}$$

where $(\beta_{x,y}, \alpha_{x,y}, \gamma_{x,y})$ represent the transversal optical functions from the Courant-Snyder parametrization. Both transversal planes are assumed to be uncorrelated and the transverse emittance ratio is set to unity. The initial transversal emittance was set to $\varepsilon_{x,y} = 1$ μmrad. The longitudinal position coordinate is distributed uniformly in the ring to resemble the coasting beam, whereas the momentum spread is modeled with a Gaussian distribution with an rms value of $\sigma_p = 0.5 \times 10^{-3}$, which is the value listed in Table I. After initialization, the particles were tracked for 10^4 turns to let the distribution converge to a stationary distribution for a given value of S. The horizontal projection of the initial beam (before excitation) is depicted in Fig. 11. The ramping of the sextupoles was not introduced adiabatically as it was done in the experiment, nevertheless

[1]This means that a sudden phase jump in adjacent phase differences are never greater than π by adding $2\pi k$ for some integer k. This signal processing routine is available in the standard numpy library [35].

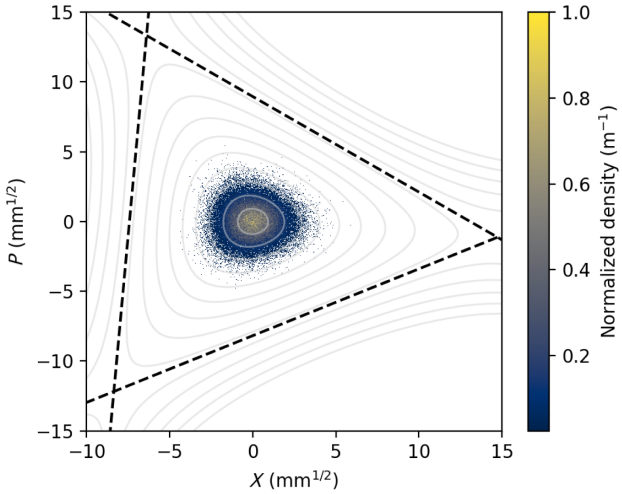

FIG. 11. Beam distribution after 10^4 turns before excitation starts. The beam was initialized with $\varepsilon_{x,y} = 1$ μmrad.

during the initial 10^4 turns the residual coherent oscillation of the beam centroid is damped due to decoherence. Then the particles experienced the kicks from the external stimulus signal. The strength of the excitation for the simulations was set to 58 nrad.

The stimulus from the measurement is modeled with a frequency chirped signal with a linear frequency sweep. The initial and end frequencies are chosen such that the range of interest shown in Figs. 7 and 9 are included in the sweep. This frequency range corresponds to a bandwidth of $\Delta q_{\mathrm{BW}} = 0.026$ in tune space and thus $Q_{\mathrm{exc}} = n \pm q_0 - \Delta q_{\mathrm{BW}}/2$ to $n \pm q_0 + \Delta q_{\mathrm{BW}}/2$ with n being the betatron sideband under investigation (here $n = 8$ or 9).

The sampling rate of both beam oscillation amplitude and stimulus signal is set to 20 samples per turn. As described in Sec. III, the sweep time of one scan is 10 s, in which 701 frequency steps are probed. The duration of the scan is determined by the time the IF filter of the VNA (70 to 100 Hz) requires to resolve the stimulus frequency component for each measurement point. This translates to approximately 3.1×10^4 turns per measurement point (2.17×10^7 turns in total). With the available computing resources and the GPU implementation offered by XSUITE, we are able to easily track 2.17×10^7 turns in total under a computing time of approximately 3.5 to 6 h for each scan.

The simulated beam oscillation amplitude is then analyzed together with the input stimulus signal. The magnitude A and phase θ of a frequency component f in the signal S_2 with regard to the excitation signal S_1 is given by

$$A = |I_2|/|I_1|, \tag{18}$$

$$\theta = \arctan\frac{\Im I_1}{\Re I_1} - \arctan\frac{\Im I_2}{\Re I_2}, \tag{19}$$

with

$$I_{1,2} = \int_{t_1}^{t_2} S_{1,2}(t) e^{i2\pi f t} \mathrm{d}t. \tag{20}$$

With the help of Eqs. (18) and (19), the measured curves are recovered from the simulation. The signal S_2 is in our experiment delivered by the capacitive pick-up electrodes and is up to a proportionality constant equivalent to the beam centroid oscillation. The signal S_2 used for evaluation of the simulation results is likewise given by the simulated transverse centroid oscillation. In the data analysis, the recovered phase given by Eq. (19) is intentionally unwrapped to avoid artificial discontinuities at $\theta = \pm\pi$.

A. Simulation results

1. Upper ninth betatron sideband

The results from the simulation are shown in Fig. 12. The splitting behavior is visible, although one can recognize that the threshold of S at which this happens is lower than in the measurement. The curves illustrated in Fig. 12 show qualitative agreement with the measurements depicted in Fig. 7 for $S \geq 25$ m$^{-1/2}$. One important addition by the simulation is the capability to fully recover the phase, which is shown in the lower panel of Fig. 12. The phase relation between driving excitation and centroid oscillations exhibits a change of $\pm\pi$ at the two visible dips, respectively. Such behavior is known to indicate resonance in the context of driven oscillators.

To understand the nature of the splitting of the measured spectra, the phase space dynamics is investigated in the simulations. The final particle distribution shown in Fig. 13 reveals that the beam core is considerably depleted as consequence of the BTF excitation. From the simulation results, we can also recover the time evolution of the particle distribution. An animated version of Fig. 13 is included in Supplemental Material [[38]]. To identify the

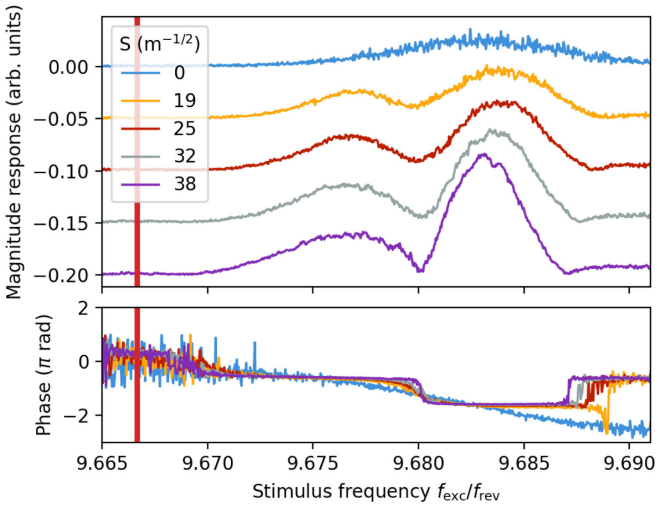

FIG. 12. Simulated beam response of a sextupole strength scan with chromaticity corrected. No particle loss is observed.

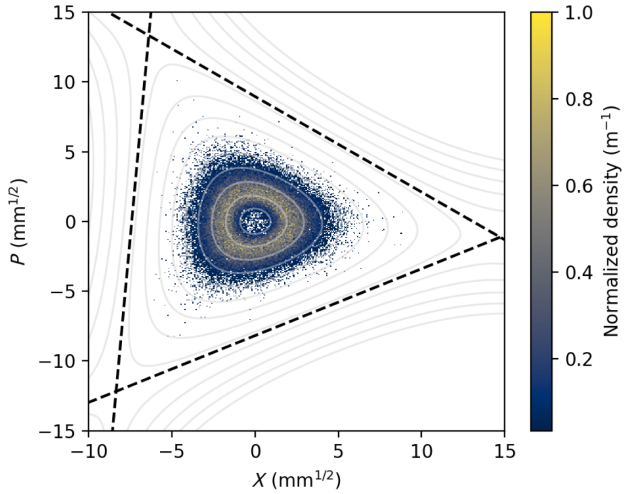

FIG. 13. Resulting particle density distribution after simulated BTF measurement for the ninth betatron upper band. The sextupole strength is $S = 25$ m$^{-1/2}$ and the simulation comprises 10^5 particles. The black line shows the separatrix from the Kobayashi theory. Dispersive and closed orbit offsets have been corrected to center the phase space. The optical functions at the observation point $s = 0$ are listed in Table III.

moment at which the core is depleted, the evolution of the effective energy distribution by means of the Hamiltonian H is shown in Fig. 14. When the excitation frequency crosses the visible dip, the average effective energy is increased and the low energy regime (core) starts to deplete.

2. Lower eighth betatron sideband

The scan around the lower eighth betatron band was simulated as well. The results of the simulation are shown in Fig. 15 and qualitative behavior is reproduced. The magnitude of the response splits in different regions.

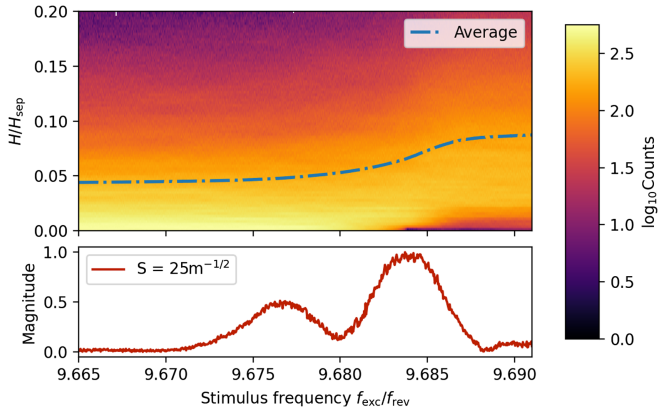

FIG. 14. Effective Hamiltonian distribution (top) and simulated BTF measurement (bottom) as a function of the excitation frequency (time of the BTF scan) for $S = 25$ m$^{-1/2}$. The Hamiltonian distribution is recovered from a sample of 10^4 particles. The blue dashed line represents the average normalized effective energy.

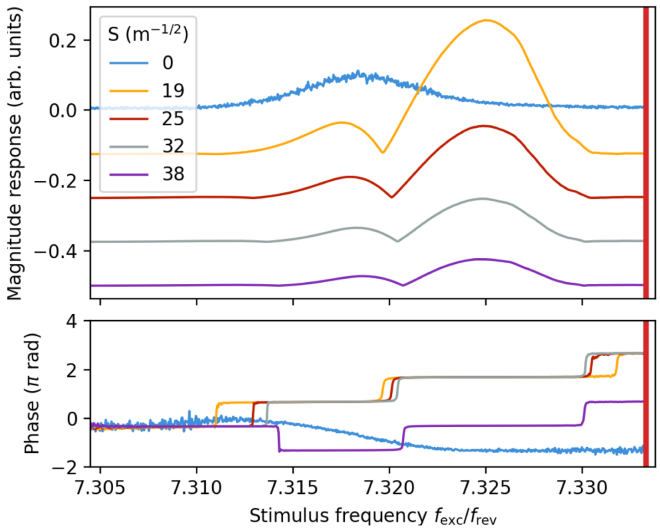

FIG. 15. Simulated beam response of a sextupole strength scan. The chromaticity was fully corrected for this simulation. The magnitude response for the $S = 0$ was magnified by a factor 100.

The phase of the signal shows a similar behavior as for the previous case where the ninth upper betatron band was investigated. There are three visible phase jumps, one notably at the visible dip in the spectrum. With the results from the simulation, the particle and the effective energy distributions were closely investigated. An animation is provided in Supplemental Material [38] and reveals interesting details of the evolution of the particle distribution during the excitation process. The resulting distribution density is illustrated in Fig. 16. The distribution is shown at

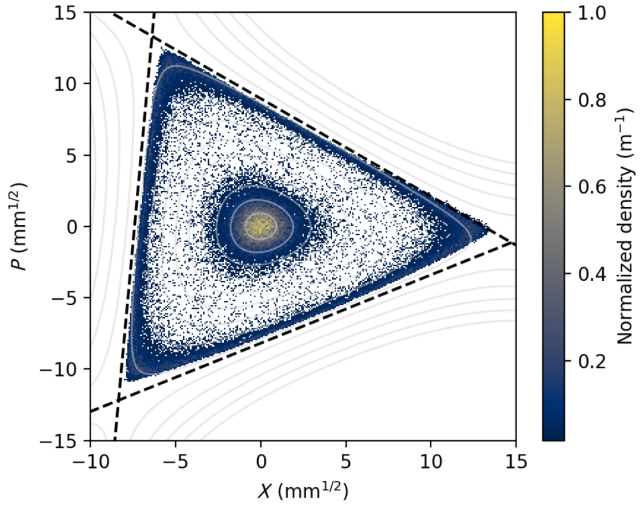

FIG. 16. Resulting particle density distribution after simulated BTF measurement at the lower eighth betatron sideband. The sextupole strength is $S = 25$ m$^{-1/2}$ and the simulation comprises 10^5 particles. The black line shows the separatrix from the Kobayashi theory. Dispersive and closed orbit offsets have been corrected to center the phase space. The optical functions at the observation point $s = 0$ are listed in Table III.

TABLE III. Optical functions at the start of the lattice (see Fig. 5). The distributions shown in Figs. 13 and 16 are shown at this point. The last value corresponds to the phase of the virtual sextupole [see Eq. (6)].

Parameter	Value
(β_x, α_x)	(5.14 m, −0.04)
(D_x, D_p)	(4.13 m, 0.67)
$(x_{\mathrm{CO}}, p_{\mathrm{CO}})$	(4 mm, −0.16 mrad)
(β_y, α_y)	(7.06 m, 1.10)
μ_S	−75.4 mrad

the same observation point as Fig. 13 (optical functions are shown in Table III). Dispersive and closed orbit offsets have been corrected as well. One recognizes that through the external stimulus particles diffuse toward the edge of the separatrix creating a halo. The simulation yields considerable particle extraction. The highest extraction yield starts at $S = 19\ \mathrm{m}^{-1/2}$ with 23% of particle loss and decreases by approximately 2% for each S step until 17.4%. For the case when the sextupoles were turned off ($S = 0$), there was no observed particle loss, as expected. In the measurement in contrast, there was no considerable particle loss observed.

The creation of the halo can also be understood by investigating closer the evolution of the effective energy distribution and this is illustrated in Fig. 17. One recognizes that through the excitation process, the distribution of the energy broadens and eventually splits, leaving an empty space between core and halo (see Fig. 16). Moreover, the influence of the sweep direction has been simulated. For the simulation near f_β^{9+}, the sweep direction was inverted and the resulting distribution is equivalent to the results shown in Fig. 16. In the same way, inverting the sweep direction of the scan near f_β^{8-} produces a hollow beam as shown in Fig. 13.

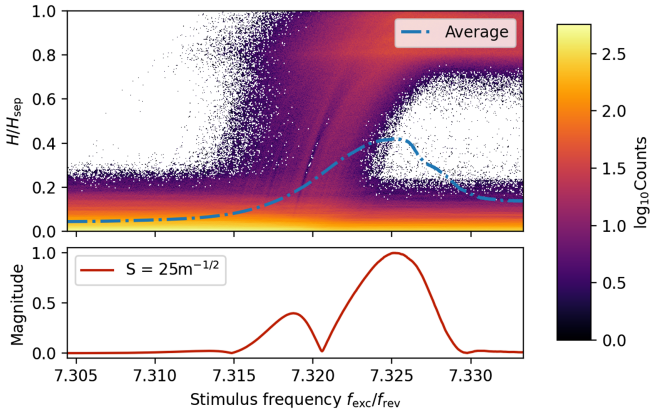

FIG. 17. Effective Hamiltonian distribution (top) and simulated BTF measurement (bottom) as a function of the excitation frequency (time of the BTF scan) for $S = 25\ \mathrm{m}^{-1/2}$. The Hamiltonian distribution is recovered from a sample of 10^4 particles. The blue dashed line represents the average normalized effective energy.

A parallel simulation study with MAPTRACK [39] was pursued. This study provides further analysis of single particle frequency behaviors as a link to the emergent collective dynamics beam response. The main results concentrate on very high excitations with kick amplitudes in the range of mrad, far beyond the range presented in this contribution. Results in [40] are derived from the investigation of a single frequency excitation near the betatron resonance and confirm the generation of a local depletion in the tune distribution. A further simulation study with a Hénon-map approach can be found in [41]. This study similarly shows evidence of the generation of a multiple peak structure in the tune distribution. We include additional simulation results in Appendix C, where two relevant parameters have been scanned: initial beam emittance and sweep duration. These simulation campaigns show how sensitive the measured signal is to the initial conditions of the system. This feature is shared among nonlinear driven oscillator systems.

V. DISCUSSION

The measured beam transfer function shows a very particular splitting behavior. The qualitative behavior at f_β^{9+} could be recovered in the simulation for $S \geq 25\ \mathrm{m}^{-1/2}$. A direct quantitative comparison was not possible. Experimental conditions are in general not completely known, e.g., the beam emittance remains experimentally undetermined. Simulations show that there is a dependence of the beam response on the emittance for the case where $S > 0$. An exemplary simulated beam response with various initial emittance values is included in Appendix C. Further, a cycle-by-cycle variation of the optics is present in the measurements and can be accentuated if the number of averaging cycles is increased. The beam response has been recorded in single cycles lasting 10 s. An exemplary set of cycle-by-cycle data is included in Appendix B.

Figure. 7 illustrates the influence of the chromaticity on the beam response. These measurements confirm that the splitting behavior in the spectrum is induced by increasing the resonance driving term S.

In the simulation, no collective effects such as impedance or particle-particle interactions were included, thus there are no damping mechanisms that could counteract the diffusion of the particle distribution. These factors could in part explain why the threshold of S, where the splitting happens appears to be higher in the measurement than the simulation. An alternative possible explanation could be that the simulated driving term S is lower than the one resulting from the real parameters in the machine. The impact of intensity-dependent effects is expected to be negligible, since the particle number is very low (see Table I), although

low energy, low intensity beams in compact machines have shown to be influenced by intrabeam scattering [42]. With these considerations in mind, we interpret the measured splitting behavior as the direct consequence of a depletion of the beam core as shown in Fig. 13. A direct confirmation of this interpretation will require a more involved experimental campaign, where the beam distribution density can be tomographed.

The discussion continues with the results obtained for the lower eighth betatron sideband. The observed qualitative behavior is similar. The measured beam response splits. In this case we can observe more peaks and dips as the resonance driving term S is increased. The measurement was performed with a higher excitation strength at 486 nrad. On the simulation side the beam response only exhibits a single prominent dip. As in the sweep near f_β^{9+}, the simulation shows that particles acquire energy as the stimulus sweeps and comes closer to the region where the tune distribution lies. Frequency differences corresponding to tune distances to the average tune higher that $\Delta q \approx 0.01$ appear to have little to no impact on the motion at low excitation strengths.

Energy gains happen even before the stimulus hits the nominal tune value. This is expected, since the amplitude-phase detuning [Eq. (9)] shifts the tune toward the third-order resonance. Prompt diffusion combined with the amplitude-phase detuning leads to a further gain in energy of particles that are in a region closer to the separatrix. A considerable amount of particles were lost in this case, whereas in the measurement there was no particle loss. The reason of this difference between simulation and measurement remains unclear. The interpretation of the results can be as well verified with a dedicated experimental campaign, where the particle distribution is tomographed to confirm if a beam core with considerable halo is generated. This is beyond the scope of this current study.

A. Summary

In this contribution, we presented the beam response of a coasting beam with a horizontal tune lying near the third-order resonance. The resonance was driven actively by exciting the resonance driving term with strong sextupoles. To the best knowledge of the authors, beam transfer functions near an actively driven resonance have not been investigated so far. These conditions are for instance, typical for resonant slow extraction from synchrotrons. The single particle dynamics was discussed and the average detuning due to the phase-amplitude term in the Kobayashi Hamiltonian was evaluated. The results of the semianalytical approach agree well with the tracking results. Further, the beam transfer function under these conditions was measured, where a scan of the sextupole strength, the excitation strength, and the excitation sweep direction were presented. All the measurements were performed at HIT with a carbon-ion beam $^{12}C^{6+}$ with $E_{\mathrm{kin}} = 124.25\,\mathrm{MeV/nucleon}$. The results show a clear splitting in the measured signal and its behavior is strongly dictated by the sextupole strength, the sweep direction, and the excitation strength. The sextupole strength scan measurements were simulated with a realistic number of turns and excitation strength but otherwise with scaled parameters. The measurement and the simulation show a good qualitative agreement for the case of the ninth upper betatron sideband. A high particle loss was observed in the simulation for the eighth lower sideband, whereas in the measurement none was recorded. The simulation results also reveal some hints for the interpretation of the measurements. The particle distribution under these conditions appear to ease the intake of energy, which finally distorts the distribution either by creating a hollow beam or by creating a halo at the edge of the separatrix. The key parameter in this set of measurements is the sweep direction in which the tunes are excited. For a sweep from resonance toward the nominal betatron resonance, particles in the core are diffused and a hollow beam is created. When sweeping in the other direction particles is able to increase their energy and therefore keep up with the excitation. This leads to the creation of a slice of halo and extraction of particles.

VI. CONCLUSION

In conclusion, the study of the beam transfer function with a beam under resonant slow extraction conditions shows rich dynamics, which are too numerous to be discussed in a single contribution. For instance, the beam transfer function can be retrieved with other types of stimuli, such as noise or delta excitations. Different stimuli will lead to different deformations of the beam distribution and hence to different beam responses. The sweep excitation method reveals that the intake of energy of the beam is non-negligible under these conditions, although the excitation strengths are low. The sweep direction determines in our experimental setup the observed beam response. As an outlook subject to experimental proof, the sweep method can offer a way to generate hollow beams or ways to populate the halo with relatively low effort.

ACKNOWLEDGMENTS

We would like to thank the whole HIT and GSI operation teams for their warm support in the measurement campaigns. We would also like to kindly thank P. Forck for his support on this project. This project has received funding from the European Union's Horizon 2020 Research and Innovation program under Grant No. 101004730. This research was supported in part through the Maxwell computational resources operated at Deutsches Elektronen-Synchrotron DESY, Hamburg, Germany.

DATA AVAILABILITY

Experimental data will be provided under request. Simulation scripts are available in Ref. [43].

APPENDIX A: BEAM OPTICS MEASUREMENTS

1. Tunes and chromaticity

The characterization of the beam optics at the HIT synchrotron is performed with help of the same beam response experimental setup described in Sec. III. Sextupoles were kept either turned off to measure the natural chromaticity or excited such that the generation of a resonance driving term [see Eq. (4)] is avoided but chromaticity is corrected. The transversal tunes were deduced by fitting a Lorentzian to the beam response measurement to extract $f_\beta^{n\pm}$ as described in [31]. The transversal chromaticity of the machine was measured by introducing an offset of the frequency of the rf cavity Δf_{HF}. An exemplary set of measurements near the upper ninth betatron sideband is shown in Fig. 18. The resulting transversal tune shifts as a function of the rf cavity frequency offset are shown in Figs. 19 and 20. The natural and corrected chromaticity setups are shown. The slip factor η was deduced by the determination of the synchrotron frequency. This was performed by determining the position of synchrotron satellites, which results in

$$f_s = (828 \pm 28)\ \mathrm{Hz}. \tag{A1}$$

The voltage of the rf cavity is $V_{\mathrm{HF}} = 464.93\ V$. Finally, the momentum spread of the beam was deduced by observing the width of the measured frequency peak at the second harmonic of the revolution frequency. This was recorded by a spectrum analyzer. The results are listed in Table I.

2. Closed orbit

The closed orbit was diagnosed with the available beam position monitors. The calculated orbit with the set of orbit correctors and the measurements is shown in Fig. 21, six in total. The readouts agree well with the expected orbit but

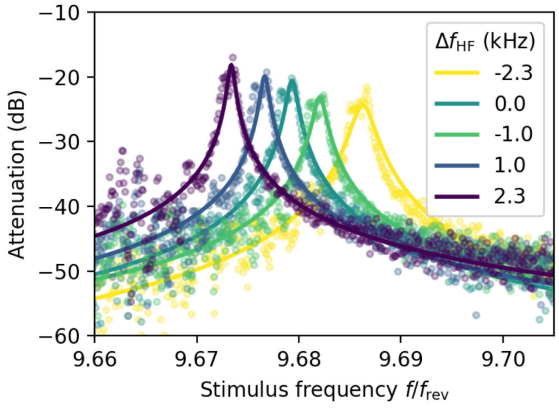

FIG. 18. Exemplary recorded data (colored dots) and Lorentzian fits (solid curves) of the horizontal ninth betatron sideband without sextupoles. Each color corresponds to the frequency shift set to the rf cavity.

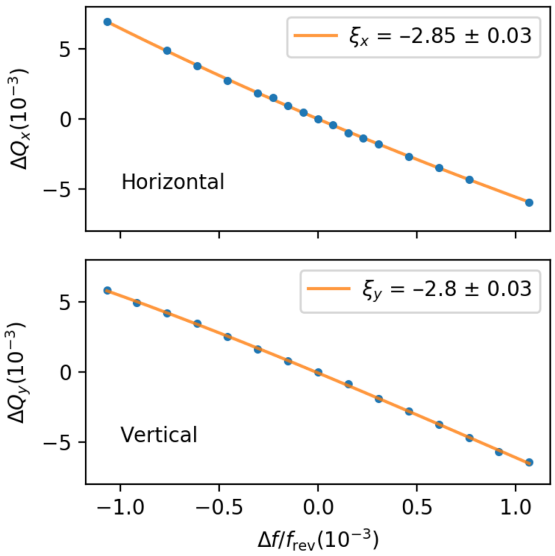

FIG. 19. Transversal tune offset as a function of the rf cavity offset for a machine without sextupoles. Blue dots are the measured data and the orange solid curve is a third-order polynomial fit. The natural linear chromaticity component deduced from the data is shown.

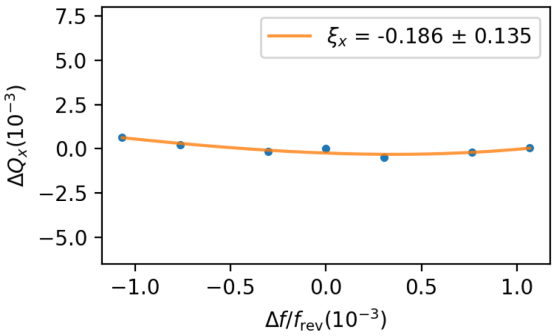

FIG. 20. Horizontal tune offset as a function of the rf cavity offset for a machine with corrected chromaticity. Blue dots are the measured data, and the orange solid curve is a third-order polynomial fit. The linear term is fully corrected.

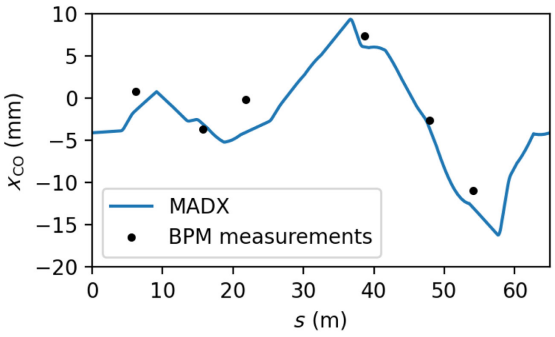

FIG. 21. Horizontal closed orbit (solid curve) calculated with MADX [34] and the corrector settings. The measured beam position monitor readings are displayed as dots.

for one value. This is probably due to a miscalibration of the monitor.

APPENDIX B: ADDITIONAL BEAM RESPONSE MEASUREMENTS

1. Lower ninth betatron sideband

The beam response was measured near f_β^{9-} with an excitation strength of 486 nrad. The amplitude and phase are shown in Fig. 22. Note that the close resemblance to the results presented in Fig. 9. The resonance is illustrated on the right as a red vertical line. All relevant experimental parameters have been reported in Sec. III.

2. Shot-to-shot data

The data presented in Sec. III are the average of consecutive sweep scans over consecutive machine cycles (shots). An example showing the shot-by-shot recorded data for the averaging is shown in Fig. 23. Observe that through the averaging the width of the peaks is artificially widened.

3. Beam response meaurement at GSI

A measurement campaign was dedicated to corroborate the results presented in Sec. III. This was made by performing similar experiments at the GSI in two shifts: May 8 and June 8, 2022. The experimental setup at SIS18 has been described multiple times and can be found easily in several publications. A quick reference search can be kick-started with [44].

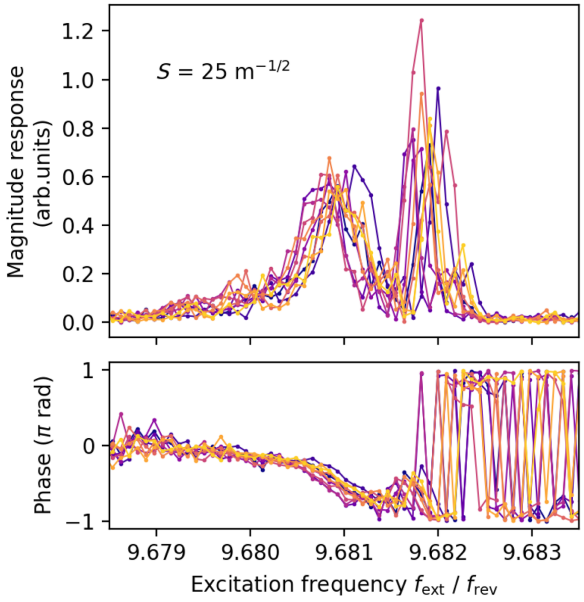

FIG. 23. Measurement of the beam response at upper ninth betatron sideband. The shot-by-shot data of 10 records are shown.

a. Sextupole strength scan

A sextupole strength scan was performed with an unbunched $^{238}U^{73+}$ beam with $E_{kin} = 900\,\mathrm{MeV/nucleon}$. The measured tunes lie at $(Q_x, Q_y) = (4.319, 3.275)$. The chromaticity at this optics was $(\xi_x, \xi_y) = (-5.66(6), -4.8(2))$, where the value in the parenthesis corresponds to the uncertainty of the last digit. The results of the scan are shown in Fig. 24. Similar to the results presented in Figs. 9 and 7, the increase of the resonance driving term, in

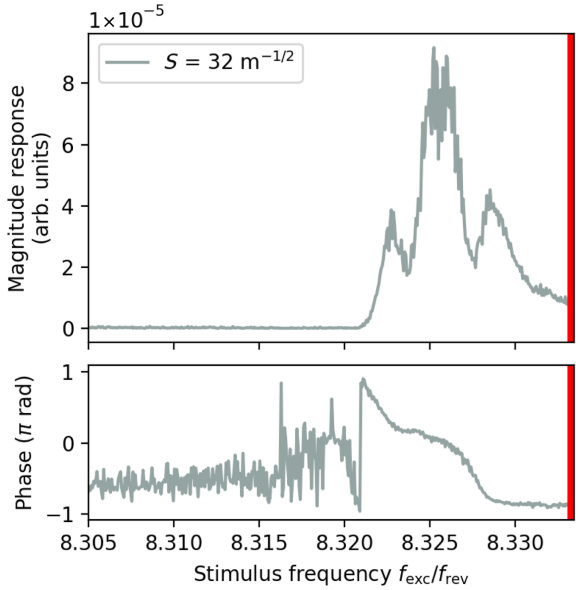

FIG. 22. Measurement of the beam response at lower ninth betatron sideband. The measured response is similar to what is observed at the lower eighth presented in Fig. 9.

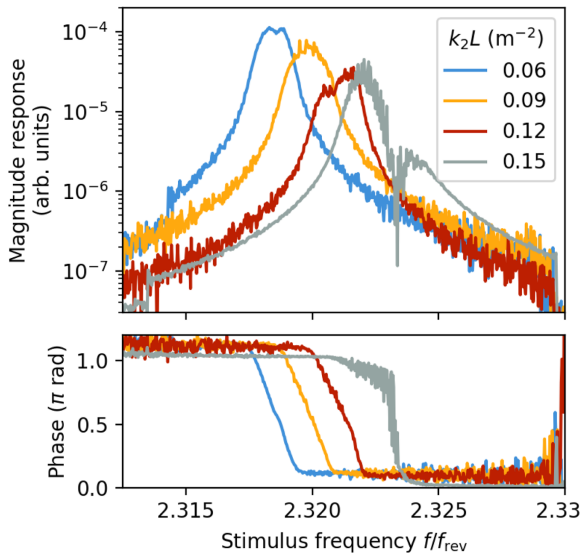

FIG. 24. Measurement of the beam response at upper second betatron sideband. A sextupole strength scan was performed and is analogous to the results presented in Figs. 7 and 9.

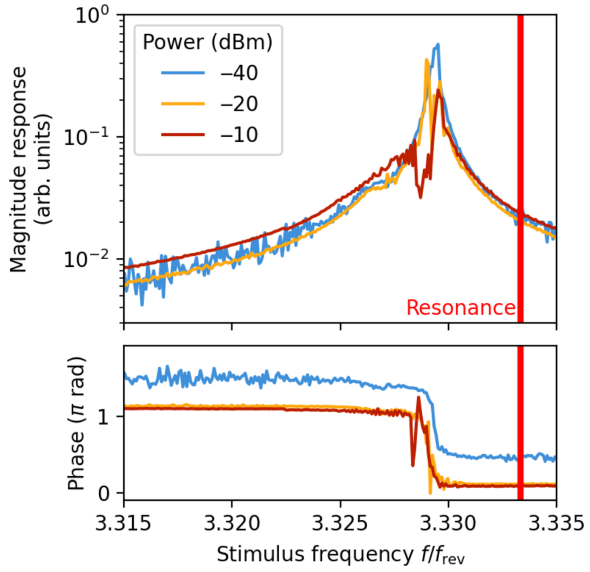

FIG. 25. Measurement of the beam response at upper third betatron sideband. An excitation strength scan was performed analogous to the results presented in Fig. 10.

this setup parameterized by k_2L, leads to a noticeable dip in the beam response.

b. Excitation strength scan

A sextupole strength scan was performed with an unbunched $^{40}Ar^{10+}$ beam with $E_{kin} = 150$ MeV/nucleon. The results are shown in Fig. 25. The behavior observed in Fig. 10 is confirmed for this setup. The higher the excitation strength of the sweep is, the deeper the dip imprints is in the measured signal. The measured tunes lie at $(Q_x, Q_y) = (4.329, 3.285)$, with a negligible uncertainty. The chromaticity at this optics was $(\xi_x, \xi_y) = (-5.491(1), -5.293(6))$, where the value in the parenthesis corresponds to the uncertainty of the last digit.

APPENDIX C: ADDITIONAL SIMULATION RESULTS

1. Emittance scan

Simulation results with different parameter scans have been performed. Emittance, a parameter which could not be deduced in the experimental setup, has been scanned. The results are shown in Fig. 26. The beam response for very low emittances changes considerably. The resulting beam distribution is still consistent with the results presented in Sec. IV, namely, a hollow beam.

2. Sweep velocity scan

The velocity of the sweep also influences the beam response. The faster the excitation sweeps over the tune, the lower the deformation of the beam distribution is.

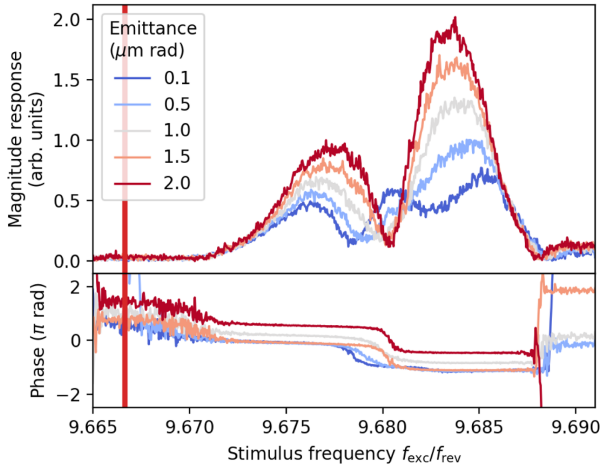

FIG. 26. Simulation of the beam response at upper ninth betatron sideband for different initial emittance values.

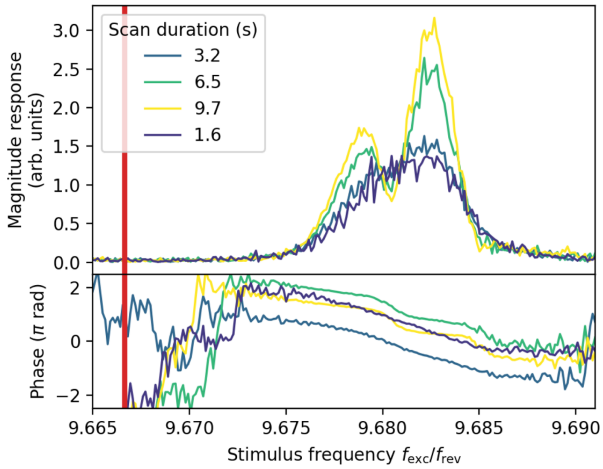

FIG. 27. Simulation of the beam response at upper ninth betatron sideband for different sweep velocities.

An exemplary scan is shown in Fig. 27. For very fast scans, the double peak disappears.

[1] Y. Kobayashi and H. Takahashi, Improvement of the emittance in the resonant ejection, in *Proceedings of the 6th International Conference High Energy Accelerators, Cambridge, MA* (1967), pp. 347–351, https://inspirehep.net/literature/921089.

[2] M. Pullia, Synchrotrons for hadrontherapy, Rev. Accel. Sci. Techol. **2**, 157 (2009).

[3] H. Tsujii, S. Minohara, and K. Noda, Heavy-particle radiotherapy: System design and application, Rev. Accel. Sci. Techol. **02**, 93 (2009).

[4] R. Singh, P. Forck, and S. Sorge, Reducing fluctuations in slow-extraction beam spill using transit-time-dependent tune modulation, Phys. Rev. Appl. **13**, 044076 (2020).

[5] M. Tomizawa, M. Yoshizawa, K. Chida, J. Yoshizawa, Y. Arakaki, R. Nagai, A. Mizobuchi, A. Noda, K. Noda,

M. Kanazawa, A. Ando, H. Muto, and T. Hattori, Slow beam extraction at TARN II, Nucl. Instrum. Methods Phys. Res., Sect. A **326**, 399 (1993).

[6] K. Noda, M. Kanazawa, A. Itano, E. Takada, M. Torikoshi, N. Araki, J. Yoshizawa, K. Sato, S. Yamada, H. Ogawa, H. Itoh, A. Noda, M. Tomizawa, and M. Yoshizawa, Slow beam extraction by a transverse RF field with AM and FM, Nucl. Instrum. Methods Phys. Res., Sect. A **374**, 269 (1996).

[7] K. Noda, T. Furukawa, S. Shibuya, M. Muramatsu, T. Uesugi, M. Kanazawa, M. Torikoshi, E. Takada, and S. Yamada, Source of spill ripple in the rf-ko slow-extraction method with fm and am, Nucl. Instrum. Methods Phys. Res., Sect. A **492**, 241 (2002).

[8] K. Noda, T. Furukawa, S. Shibuya, T. Uesugi, M. Muramatsu, M. Kanazawa, E. Takada, and S. Yamada, Advanced rf-ko slow-extraction method for the reduction of spill ripple, Nucl. Instrum. Methods Phys. Res., Sect. A **492**, 253 (2002).

[9] C. K. *et al.*, Slow extraction techniques at the marburg ion-beam therapy centre, in *Proceedings of the 9th International Particle Accelerator Conference, IPAC-2018, Vancouver, BC Canada* (JACoW, Geneva, Switzerland, 2018), Vol. 1.

[10] T. Yamaguchi, Y. Okugawa, T. Shiokawa, T. Kurita, and T. Nakanishi, Slow beam extraction from a synchrotron using a radio frequency knockout system with a broadband colored noise signal, Nucl. Instrum. Methods Phys. Res., Sect. B **462**, 177 (2020).

[11] T. Shiokawa, Y. Okugawa, T. Kurita, and T. Nakanishi, Slow beam extraction method from synchrotron for uniform spill and fast beam switching using an rf knockout method of multi-band colored noise signal–pop experiment and simulation, Nucl. Instrum. Methods Phys. Res., Sect. A **1010**, 165560 (2021).

[12] E. Cortés García, E. Feldmeier, M. Galonska, C. Schömers, M. Hun, S. Brons, R. Cee, S. Scheloske, A. Peters, and T. Haberer, Optimization of the spill quality for the hadron therapy at the Heidelberg ion-beam therapy centre, Nucl. Instrum. Methods Phys. Res., Sect. A **1040**, 167137 (2022).

[13] P. J. Niedermayer, R. Singh, G. Franchetti, E. C. C. García, E. Feldmeier, and T. Haberer, Investigation of micro spill in RF KO extraction using tailored excitation signals, J. Phys. Conf. Ser. **2687**, 052029 (2024).

[14] A. Dragt, *Lie Methods for Nonlinear Dynamics with Applications to Accelerator Physics* (University of Maryland, Maryland, USA, 2018), https://www.physics.umd.edu/dsat/.

[15] A. W. Chao, *Special Topics in Accelerator Physics* (World Scientific, Hackensack, 2022), pp. 1–716, illustrations, diagrams.

[16] L. Badano, M. Benedikt, P. J. Bryant, M. Crescenti, P. Holy, A. T. Maier, M. Pullia, S. Rossi, P. Knaus, and CERN-TERA Foundation-MedAustron Oncology-2000 Collaboration, Proton-ion medical machine study (PIMMS), 1 (1999).

[17] D. D. Caussyn, M. Ball, B. Brabson, J. Collins, S. A. Curtis, V. Derenchuck, D. DuPlantis, G. East, M. Ellison, T. Ellison, D. Friesel, B. Hamilton, W. P. Jones, W. Lamble, S. Y. Lee, D. Li, M. G. Minty, T. Sloan, G. Xu, A. W. Chao, K. Y. Ng, and S. Tepikian, Experimental studies of nonlinear beam dynamics, Phys. Rev. A **46**, 7942 (1992).

[18] W. Herr, Mathematical and numerical methods of nonlinear beam dynamics, in *Proceedings of the 2018 CERN Accelerator School Course on Numerical Methods for Analysis, Design and Modelling of Particle Accelerators, Thessaloniki, Greece* (2020), arXiv:2006.09052.

[19] A. Bazzani, G. Servizi, E. Todesco, and G. Turchetti, *A Normal Form Approach to the Theory of Nonlinear Betatronic Motion, CERN Yellow Reports: Monograph* (CERN, Geneva, 1994).

[20] P. Niedermayer, Average amplitude and phase detuning near driven 3rd integer resonance, arXiv:2403.17629.

[21] C. Hayashi, *Nonlinear Oscillations in Physical Systems* (Princeton University Press, Princeton, 2014).

[22] B. V. Chirikov, A universal instability of many-dimensional oscillator systems, Phys. Rep. **52**, 263 (1979).

[23] A. Bazzani, F. Capoani, and M. Giovannozzi, Analysis of adiabatic trapping phenomena for quasi-integrable area-preserving maps in the presence of time-dependent exciters, Phys. Rev. E **106**, 034204 (2022).

[24] T. Hiraiwa, K. Soutome, and H. Tanaka, Formulation of electron motion in a storage ring with a betatron tune varying with time and a dipole shaker working at a constant frequency, Phys. Rev. Accel. Beams **24**, 114001 (2021).

[25] R. Singh, O. Boine-Frankenheim, O. Chorniy, P. Forck, R. Haseitl, W. Kaufmann, P. Kowina, K. Lang, and T. Weiland, Interpretation of transverse tune spectra in a heavy-ion synchrotron at high intensities, Phys. Rev. ST Accel. Beams **16**, 034201 (2013).

[26] P. Görgen, O. Boine-Frankenheim, and W. Fischer, Beam transfer functions for relativistic proton bunches with beam–beam interaction, Nucl. Instrum. Methods Phys. Res., Sect. A **777**, 43 (2015).

[27] A. W. Chao, Physics of collective beam instabilities in high-energy accelerators (1993), https://www.slac.stanford.edu/~achao/wileybook.html.

[28] K. Y. Ng, *Physics of Intensity Dependent Beam Instabilities* (World Scientific, Singapore, 2005), https://www.worldscientific.com/doi/pdf/10.1142/5835.

[29] J. Berg and F. Ruggiero, Landau damping with two-dimensional betatron tune spread, CERN, Technical Report No. CERN SL-AP96-71, 1996.

[30] C. Tambasco, T. Pieloni, J. Barranco, X. Buffat, T. Levens, E. Métral, and B. Salvachua, Beam transfer function measurements used to probe the transverse landau damping at the lhc, Phys. Rev. Accel. Beams **23**, 071002 (2020).

[31] P. Forck, Beam instrumentation and diagnostics, arXiv:2009.10411.

[32] H. Eickhoff, D. Bhne, T. Haberer, B. Schlitt, P. Spiller, G. Darmstadt, J. Debus, R. Clinic, and A. Dolinskii, The proposed dedicated ion beam facility for cancer therapy at the clinic in Heidelberg, in *Proceedings of the 7th European Particle Accelerator Conference, EPAC-2000, Vienna, Austria* (JACoW, Geneva, Switzerland, 2000).

[33] T. Haberer, W. Becher, D. Schardt, and G. Kraft, Magnetic scanning system for heavy ion therapy, Nucl. Instrum. Methods Phys. Res., Sect. A **330**, 296 (1993).

[34] L. Deniau, H. Grote, G. Roy, and F. Schmidt, *The MAD-X Program (Methodical Accelerator Design) Version 5.08.01 User's Reference Manual* (CERN, Geneva, Switzerland, 2022), https://madx.web.cern.ch/madx/.

[35] C. R. Harris, K. J. Millman, S. J. van der Walt, R. Gommers, P. Virtanen, D. Cournapeau, E. Wieser, J. Taylor, S. Berg, N. J. Smith, R. Kern, M. Picus, S. Hoyer, M. H. van Kerkwijk, M. Brett, A. Haldane, J. F. del Río, M. Wiebe, P. Peterson, P. Gérard-Marchant, K. Sheppard, T. Reddy, W. Weckesser, H. Abbasi, C. Gohlke, and T. E. Oliphant, Array programming with NumPy, Nature (London) **585**, 357 (2020).

[36] P. Niedermayer and R. Singh, Excitation of nonlinear second order betatron sidebands for knock-out slow extraction at the third-integer resonance, Phys. Rev. Accel. Beams **27**, 082801 (2024).

[37] G. Iadarola, A. Abramov, P. Belanger, X. Buffat, R. D. Maria, D. Demetriadou, L. Deniau, D. D. Croce, P. Hermes, P. Kicsiny, P. Kruyt, A. Latina, L. Mether, P. Niedermayer, K. Paraschou, T. Pieloni, M. Seidel, G. Sterbini, F. V. der Veken, L. van Riesen-Haupt, and S. Łopaciuk, Xsuite: an integrated beam physics simulation framework, in *Proceedings of the 68th Advanced Beam Dynamic Workshop High-Intensity High-Brightness Hadron Beams (HB'23)* (JACoW, Geneva, Switzerland, 2024), Vol. 68, pp. 73–80.

[38] See Supplementak Material at http://link.aps.org/supplemental/10.1103/PhysRevAccelBeams.27.124001 for short animations of the excitation process of the upper ninth and the lower eighth betratron sidebands under resonant slow extraction conditions.

[39] F. M. Velotti, Maptrack, https://gitlab.cern.ch/abt-optics-and-code-repository/simulation-codes/maptrack.

[40] R. Taylor, Slow extraction: Upgrades for next ion medical machines at FLASH timescales (2024), http://cds.cern.ch/record/2915795/files/.

[41] P. Niedermayer and R. Singh, Transverse excitation and applications for beam control, in *Proceedings of the 13th International Particle Accelerator Conference, IPAC-2022* (JACoW, Geneva, Switzerland, 2022), pp. 251–253.

[42] M. Beutelspacher, M. Grieser, K. Noda, D. Schwalm, and A. Wolf, Dispersive electron cooling experiments at the heavy ion storage ring TSR, Nucl. Instrum. Methods Phys. Res., Sect. A **512**, 459 (2003).

[43] https://github.com/hibtc/btf-simulation

[44] D. Ondreka, C. Dimopoulou, H. Hüther, H. Liebermann, J. Stadlmann, and R. Steinhagen, Recommissioning of SIS18 after FAIR upgrades, in *Proceedings of the 10th International Particle Accelerator Conference, IPAC-2019, Melbourne, Australia,* (JACoW, Geneva, Switzerland, 2019), MOPTS035.